Radio Science, Volume ???, Number , Pages 1–12,

Passive over-the-horizon radar with WWV and the first station of the Long Wavelength Array

J. F. Helmboldt,[1] T. E. Clarke,[1] J. Craig,[2] S. W. Ellingson,[3] J. M. Hartman,[4,5] B. C. Hicks,[1] N. E. Kassim,[1] G. B. Taylor,[2,6] & C. N. Wolfe[3]

We present a new passive, over-the-horizon (OTH) radar system consisting of the transmitters for the HF radio station WWV and the dipole-antenna array that comprises the first station of the Long Wavelength Array (LWA), or "LWA1." We demonstrate that these two existing facilities, which are operated for separate purposes, can be used together as a relatively powerful bistatic, HF radar, capable of monitoring the entire visible sky. In this paper, we describe in detail the techniques used to develop all-sky, OTH radar capability at 10, 15, and 20 MHz. We show that this radar system can be a powerful tool for probing ionospheric structure by quantifying the degree of "tilt" effected by ionospheric density gradients along the ray paths, including the effect this has on OTH geolocation. The LWA1+WWV radar system appears to be especially adept at detecting and characterizing structures associated with sporadic-E. In addition, we also demonstrate how this system may be used for long-distance, OTH mapping of terrain/ocean HF reflectivity.

1. Introduction

High-frequency (HF; 3–30 MHz) radars have been used for decades for several applications. Operating as both monostatic and bistatic radar systems, ionosondes have been and continue to be used to sound the ionosphere, probing the evolution of the ionospheric electron density profile. They remain valuable assets for both basic ionospheric research and as support systems for operational radars. So-called over-the-horizon (OTH) radars were developed after World War II to exploit the ionosphere as a "virtual mirror" that could reflect both outgoing and returning HF signals to track OTH targets. OTH radars remain a valuable long-distance surveillance tool used, for example, to monitor illegal narcotics trafficking in the Caribbean [see *Headrick and Thomason*, 1998, for a more thorough discussion].

As detailed by *Headrick and Thomason* [1998], the transmitter portion of operational OTH radars are particularly cumbersome and difficult to develop given the large size required for high-power HF transmitting antennas. This paper details efforts to develop a so-called "passive" radar capability in the HF regime that uses existing transmitters, whose operation is independent from that of the radar system itself. This concept was successfully employed to study high-latitude ionospheric scattering events by *Meyer and Sahr* [2004] using FM stations at $\sim$100 MHz.

Here, the transmitters used are those of the National Institute of Standards and Technology (NIST) radio station located near Ft. Collins, Colorado, call-sign WWV. WWV broadcasts the current time at five different HF frequencies. Relatively nearby, but over the horizon is the newly operational first station of the Long Wavelength Array (LWA), referred to as LWA1 [*Taylor et al.*, 2012; *Ellingson et al.*, 2012]. The full LWA will consist of 52 stations spread throughout the state of New Mexico designed to work as a large HF/VHF interferometer/telescope for imaging cosmic sources [*Taylor et al.*, 2006]. Each station will be a roughly 100-m wide phased array of

[1]US Naval Research Laboratory, Code 7213, Washington, DC 20375, USA.
[2]Department of Physics and Astronomy, University of New Mexico, Albuquerque NM, 87131, USA.
[3]Bradley Dept. of Electrical & Computer Engineering, Virginia Tech, Blacksburg, VA 24061.
[4]Jet Propulsion Laboratory, California Institute of Technology, Pasadena, CA, USA.
[5]NASA Postdoctoral Program Fellow
[6]Greg Taylor is also an Adjunct Astronomer at the National Radio Astronomy Observatory.

0048-6604/13/$11.00

256 crossed-dipole antennas. The unique capability of LWA1 to image the entire sky rather than point at one particular location makes it a particularly flexible radar receiving system. We will demonstrate that when used together, LWA1 and WWV constitute a powerful OTH radar system that could potentially operate continuously and relatively cheaply. We describe the techniques involved (Sec. 2–3) as well as examples of possible applications of the system (Sec. 4) and future capabilities as more LWA stations are added (Sec. 5).

2. LWA1 and WWV

2.1. LWA1

LWA1 is the first station of the planned LWA which will consist of more than 50 similar stations, acting together as an HF/VHF, interferometric telescope. Like LWA1, each station will consist of 256 cross-dipole antennas capable of operating between 10 and 88 MHz arranged in a quasi-random pattern spanning roughly 100 m designed to minimize sidelobes. Each dipole antenna consists of a wire-grid "bow-tie" mounted to a central mast with arms angled downward at a roughly 45° angle. This design maximizes sensitivity/throughput over the entire observable sky. For a detailed discussion of the antenna design, see *Hicks et al.* [2012]. LWA1 is currently being operated as an independent telescope/observatory located at 34.070°N, 107.628°W and is described in detail by *Taylor et al.* [2012] and *Ellingson et al.* [2012], including a description of the calibration of the array using bright cosmic sources and an additional "outrigger" antenna located roughly 300 m east of the array center.

The antennas can be operated as a single phased array with up to four simultaneous beams. Each beam can use up to two tunings, each with a passband having up to 16 MHz of usable bandwidth. Independent from the beam-forming mode, LWA1 also has a transient buffer (TB) mode that records the individual output from each antenna, allowing one to beam-form to any point on the sky after the fact and making all-sky imaging possible.

The TB can be operated in one of two modes. The first is a wide-band mode (TBW) which captures 61.2 ms of the raw signal from each antenna at a sampling rate of 196 Msps with 12 bits per sample. With this data, one has access to the full bandwidth accessible by the antennas. However, since the data volume is so large (>9 GB per capture), it takes more than five minutes to write each capture to disk and thus cannot be run in a continuous way. Conversely, the narrow-band mode (TBN) tunes each antenna signal to a specified central frequency with a sampling rate of up to 100 ksps with up to 67 kHz of usable bandwidth. The data rate for this mode is small enough that it can be run continuously for up to roughly 20 hours before filling the available disk space. Examples of all-sky images of cosmic sources made using TBN data and the LWA1 Prototype All-Sky Imager [PASI; *Ellingson et al.*, 2012] can be found at `http://www.phys.unm.edu/~lwa/lwatv.html`, which is updated in near real time as data are taken. An example of an image of the entire visible sky constructed from TBN data was also presented by *Dowell et al.* [2012].

It is the two TB modes that are particularly useful for passive radar applications. Because they allow for all-sky imaging, any terrestrial transmitter whose direct signal, ground wave, or sky wave (ionospheric reflection) is observable from LWA1 can be detected and located with either TBW or TBN data. In cases where both the direct signal and the ground wave and/or sky wave are simultaneously detected (e.g., a local FM station), the transmitter signal can be obtained by beam-forming toward the transmitter and this can be used as a matched filter for obtaining ranges for the ground and/or sky wave detections according to *Meyer and Sahr* [2004]. Alternatively, because LWA1 uses its own GPS clock to time-stamp each TB sample, a transmitter with a known pulse-like signal structure like WWV (see Sec. 2.3) can also be used for passive radar with good time-of-arrival accuracy (rms variation of about 20 ns $\simeq$ 6 m).

2.2. WWV

WWV is an HF radio station that broadcasts the time from the Ft. Collins, Colorado area (40.7°N, 105.0°W; 770 km to the northeast of LWA1) at 2.5, 5, 10, 15, and 20 MHz. It has a "sister" station in Hawaii (22.0°N, 159.8°W), call-sign WWVH, which broadcasts the time at the same frequencies except 20 MHz. These stations and their signal patterns are described in great detail by *Nelson et al.* [2005]. In general, amplitude modulation of each signal is used to convey various types of information about the current universal time (UT). Here, we briefly describe those aspects of the WWV signals that are relevant to passive radar.

The transmitters for both WWV and WWVH are relatively powerful monopole antennas, each with an ERP of 10 kW for 5, 10, and 15 MHz and 2.5 kW for 2.5 and 20 MHz. The WWVH transmitters are directional with most of the power directed westward to minimize interference with WWV. Both broadcast voice announcements of the time at each frequency, modulated at either 500 or 600 Hz. They also broadcast a coded signal, modulated at 100 Hz, that transmits the UT of the current minute. There are also occasionally alarm signals transmitted, which are modulated at 2000 Hz.

We have found that the amplitude modulation schemes used for the main portions of the WWV signals described above make for rather poor matched filters. Using LWA1 observations of WWV echoes (see 2.3), we have attempted to apply the WWV signal as a matched filter to itself and found that it produces multiple peaks at different lags, making if difficult, if not impossible, to use the same techniques employed by *Meyer and Sahr* [2004] with FM stations for ranging. This is basically the result of the relatively slowly changing amplitudes of the primary constituents of the continuous WWV signal, namely the main carrier, the 100-Hz time code, and the 500/600-Hz voice announcements. For instance, within the 100-Hz time code, date bits of zero or one are indicated using constant amplitudes over intervals of 200 or 500 ms, respectively. The main carrier and voice announcements have amplitudes that are similarly temporally stable as indicated by their spectral profiles which are just as narrow as that of the 100 MHz time code (see Sec. 2.3 and Fig. 1–2).

The most useful part of both the WWV and WWVH signals for passive radar are the 5-ms pulses emitted at the beginning of each second (except on the 29^{th} and 59^{th} second of each minute). All other signals are suppressed 10 ms before the beginning of each pulse to 25 ms after the end of the pulse to help them stand out more. WWV pulses are modulated at 1000 Hz, and the WWVH pulses are modulated at 1200 Hz, making them distinct from one another. Thus, by applying the appropriate filtering techniques, one may isolate these pulses within signals received by the LWA1 antennas for different arrival times, corresponding to different ranges.

The main drawback of using the 5-ms WWV pulse for ranging is that it provides little practical capability for determining Doppler speeds. Normally with a pulsed transmitter, one can use the pulses that have a common time of flight as a time series that can be Fourier transformed to map the amount of power as a function of Doppler frequency. However, the one-second cadence of the WWV pulses implies a Nyquist limit of 0.5 Hz. At 10, 15, and 20 MHz, this maximum Doppler shift corresponds to speeds of 7.5, 5, and 3.75 m s^{-1}. While there may be OTH targets and ionospheric structures with Doppler speeds this low, there will likely be many more with higher speeds that will be aliased to lower Doppler frequencies by the coarse, one-second sampling, and it would not be possible to distinguish between these two scenarios. Therefore, in practice, obtaining Doppler speeds with the WWV pulse it not feasible.

2.3. Imaging WWV Echoes with LWA1

Since the LWA1 antennas have little if any sensitivity below 10 MHz, the bands where LWA1 and WWV overlap are 10, 15, and 20 MHz. Given the distance between WWV and LWA1, 770.0 km, the direct signal and ground wave are not detectable from LWA1. However, conditions in the ionosphere are nearly always such that a reflection of the 10 MHz signal is visible, and reflections at 15 and 20 MHz are sometimes detected. In addition, ionospheric echoes of the 10 and 15 MHz WWVH signals are often visible. Given the large distance to WWVH (5236.0 km), these reflections are almost certainly "multi-hop" reflections, that is, they have bounced between the ionosphere and the ocean/terrain several times before arriving at LWA1. Relatively speaking, the WWVH signal is typically more prominent at 15 MHz.

Examples of ionospheric echoes of both the WWV and WWVH signals are illustrated in Fig. 1 and 2. Fig. 1 shows an all-sky image made via total-power beam forming at 10 MHz with 12.0 kHz of bandwidth from a single TBW capture. For such images, complex voltages were made using an FFT of the raw signals and each antenna's voltage was multiplied by a two-dimensional array of phasers before adding them together to compute the total beam-formed power over the whole observable sky. These phasers include corrections for cable losses, unequal cable delays, and other amplitude and phase errors measured for each antenna using observations of bright cosmic sources using the outrigger antenna mentioned in Sec. 2.1. These corrections are described in more detail by *Ellingson et al.* [2012] and are included within the LWA Software Library [LSL; *Dowell et al.*, 2012].

The image displayed in Fig. 1 is a combination of the total power from the north-south and east-west dipoles, yielding the total, Stokes-I power. For these images, the ordinate and abscissa are the so-called l and m direction cosines, defined in this case to be $l = \cos e \cos a$ and $m = \cos e \sin a$, where e is the elevation above the horizon and a is the azimuth measured clockwise from north. This projection was chosen because the LWA1 beam changes very little within the l,m-plane. One should note that in this projection, elevation does not vary linearly with radius and that a source appearing extremely close to the horizon (i.e., $\sqrt{l^2 + m^2} = 1$) may in fact be at a deceptively high elevation. For instance, the strong 10 MHz echo seen in the upper left of Fig. 1 is at an elevation of 27°.

Fig. 1 also shows a time series of the amplitude of the signal beam-formed toward the approximate center of the 10 MHz echo seen in the all-sky image (marked with an ×). One can clearly see the 5-ms WWV pulse modulated at 100 Hz with an arrival time of 2.97 ms after the beginning of the second, corresponding to a distance traveled of 890 km. Because each TBW capture is set up to start at the beginning of each UT second, the 61.2 ms duration of each capture is more than enough time to detect such echoes from either WWV or WWVH. The power spectrum of this beam-formed signal is also shown in Fig. 1. The strongest part of the signal is the main carrier at 10 MHz. One can also pick out features mentioned in the description above (labeled in red) such as the 100-Hz time code, the 600-Hz voice announcement, the 1000-Hz pulse, and the 2000-Hz alarm code. Also shown is a shaded region one might use as a side-band filter to isolate the 5-ms pulse while avoiding the voice announcement and alarm codes, which is wide enough to achieve a temporal resolution of roughly 1 ms.

Fig. 2 shows the same thing as Fig. 1, but at 15 MHz, highlighting a detection of an echo from WWVH. The all-sky image shows some contribution from "second-hop" signals from WWV, those that reflected off the ionosphere, then off the ocean/terrain, then back off the ionosphere to LWA1, which are distributed around the horizon. Because of these second-hop signals, the beam-formed signal shown in the upper right panel is not as clean as that shown in Fig. 1 for WWV at 10 MHz, but the 5-ms pulse is still clearly visible. In this case, the arrival time is significantly larger, 19.8 ms (or, 5952 km), indicative of the more distant origin in Hawaii. In addition, the pulse has more cycles than the 10 MHz signal (six versus five), consistent with WWVH's pulse modulation of 1200 Hz. This can be seen more clearly in the power spectrum where the peaks from the 5-ms pulse are centered at ±1200 Hz instead of ±1000 Hz.

3. LWA1+WWV Bistatic Radar

The examples shown in Fig. 1–2 demonstrate the potential for using WWV and LWA1 as a relatively powerful bistatic HF radar, capable of probing the ionosphere and OTH targets using the ionosphere as a virtual mirror. Here, we describe the methods we have developed to do just that using both TBW and TBN data.

3.1. TBW and Multi-frequency Radar

As described above, the LWA1 TBW mode offers a unique capability to make total power images from signals spanning the entire available frequency range, 10–88 MHz, all observed simultaneously. The sacrifice one makes for this wide-band coverage is that one can only get 61.2 ms of data every five minutes or more. Fortunately, each TBW capture is timed to start at the beginning of each UT second, making it possible to detect reflections from the WWV 5-ms pulse within this short 61.2 ms window.

To isolate echoes of the 5-ms WWV pulse within TBW data, we have used the following multi-step approach. First, the format of the data dictates that one read in almost the entire 61.2-ms capture as part of any post-processing effort. A TBW binary data file is broken up into frames, each consisting of 400 samples from a single antenna. The frames are not organized by antenna ID or time; they are written out on a kind of "first-come-first-serve" basis. Because of that, all of the data for a particular antenna might be contained within the first few percent of the file, while for another, one may have to parse the entire file to retrieve all of its data. In addition, this pattern is different for each file [see *Ellingson*, 2007, for a more detailed description of the TBW system].

Because of this file structure, it is more efficient to use an FFT to filter the data for each antenna as it is read in, yielding a time series of complex voltages for each antenna once the whole file has been read. In practice, for each antenna, an FFT is applied every 1024 samples, and the resulting voltages for the frequencies closest to 10, 15, and 20 MHz (9.953,

14.93, and 19.91 MHz) are saved, giving a time series of 11,718 voltages for each band, each with a bandwidth of 4.98 MHz.

Following this, an FFT is applied to each of these time series and the resulting complex spectrum is filtered with two side-band filters illustrated in Fig. 1. An inverse FFT is then applied to each side band to yield a new complex voltage time series with a temporal sampling of 1.004 ms within which the 5-ms pulse appears as a square pulse rather than a sinusoid. For each point in this time series, a total-power beam-formed image is made over the whole sky (see Sec. 2.3), separately for each side-band and each polarization. These four images are then combined to form a single image cube that gives the total power as a function of azimuth, elevation, and time of arrival/range.

We have used three sequences of TBW captures to help illustrate the typical output of this combined radar system. These were conducted between 00:05 and 13:25 UT, May 6, 2012; between 05:05 and 14:05, May 7, 2012; and between 19:55 and 15:05 UT, September 30–31, 2012 as part of telescope commissioning efforts. Within each sequence, the captures were spaced 10 minutes apart. Fig. 3–5 show example image cubes for 10, 15, and 20 MHz, which are the first frames of three electronically available movies made from these TBW sequences. Each frame shows the total-power, all-sky map of the 5-ms pulse at different times of arrival, converted to distance traveled from 153 to 7374 km with the horizon marked with a white circle. We note again that due to the projection used to display these images (see Sec. 2.3), nearly all of the detected echoes appear as if they are at or just above the horizon, even though the typically elevation is actually about 10° and varies from a few degrees to as high as 40°. We also note that the times of flight for the detected echoes are too large for them to be ground waves from WWV.

The relatively poor range resolution afforded by the width of the 5-ms pulse is evident within these image cubes. However, one can see that the all-sky approach, when combined with range information, allows one to readily distinguish among the first-hop WWV signal (16° east of north), second-hop WWV signals at various azimuths, and the echo of the WWVH pulse (almost exactly due west). One can also see that while 10 MHz echoes are almost always visible from both WWV and WWVH, only WWVH is consistently visible at 15 MHz. Echoes of the WWV pulse are only detected some of the time at 15 and 20 MHz. This is not entirely unexpected given the large plasma frequencies and/or low angles of incidence needed to reflect 15 and 20 MHz transmissions between WWV and LWA1. The instances where the WWV signal is seen at 15 and 20 MHz are likely related to sporadic-E (E_s), which will be discussed further below.

3.2. TBN and Continuous Radar

While the multi-frequency data available with TBW captures offers a method for sounding the ionosphere, TBN observations allow one to monitor a particular ionospheric region/layer (or, OTH target) at one frequency with much better temporal coverage (i.e., one sample per second versus one every 5 minutes or more). For those readers familiar with digisonde dipole arrays, in this context, the TBW and TBN modes are analogous to the digisonde "sounding" and "sky map" modes.

In principle, one may analyze TBN observations using the same procedure described for the TBW data in Sec. 3.1. However, the differences in file structures between TBW and TBN data make it more practical to use a different but related approach with TBN data. Since the data are already filtered in TBN mode before they are written out, what is recorded are complex voltages rather than raw signals. Typically, these are written out with a sampling rate of 100 ksps (16 bits per sample), but lower sampling rates are possible. TBN binary files are broken up into frames, similar to TBW files. However, within a TBN file, a frame consists of 512 samples from a single antenna and the data for all antennas are written out together for each time stamp (although, not necessarily ordered by antenna ID). This makes it faster to read in just the time stamp of each frame until the first frame closest to the next UT second is identified. After this, due to the lower sampling rate, one can easily read all of the data for all antennas covering the next several tens of milliseconds into RAM, even with a modestly equipped desktop computer (e.g., 40 ms amounts to roughly 4 MB).

We found that rather than using the FFT/filter/inverse-FFT approach employed with the TBW data, it was faster/more efficient to apply a sliding window filter to these data as they were read in. Specifically, as the data are read in, they are up/down converted by ±1000 Hz, after which a 5-ms wide Hamming window is applied and the data within this window are aver-

aged. The Hamming window was chosen to suppress contributions from higher frequencies and is stepped at 1-ms intervals to give comparable temporal sampling to the TBW approach. This is done for the first 40 ms of each UT second, yielding 40 up- and down-converted complex voltages (i.e., at the carrier frequency ±1000 Hz) for each antenna corresponding to 40 different times of arrival for the WWV pulse. Similar to the TBW approach, the up- and down-converted voltages are imaged separately and then combined for each time of arrival. In applying this analysis to actual TBN data (see below), we found that the time stamps in the TBN files were off by 10.24 ms, a result of the time stamps being assigned after the data had been passed through the hardware filters, which have a length of 1024 samples. All times of arrival within the TBN analysis are corrected for this effect.

As a demonstration of this method, we have used a 15-minute TBN observation at 15 MHz that started at 00 UT on September 25, 2012. This time was chosen based on the results from the TBW captures, which indicated that this is a time when 15 MHz echoes from WWV are common. The analysis described above was applied to this data-set, and we have made a movie of the resulting image cubes available electronically. Note that, as mentioned in Sec. 2.2, the WWV pulse is not broadcast on the 29^{th} and 59^{th} second of each minute, which causes a "blinking" effect within this movie with a cadence of about 30 seconds. At these times, only the main 15 MHz carrier and/or the voice announcements are broadcast, so that even though echoes are detected, the arrival times are relatively meaningless without the 1000-Hz-modulated pulse.

The movie shows that the first-hop signals from WWV often have observed structure beyond a simple unresolved, point-like source. This additional structure commonly lasts for only one to a few seconds. However, there is a strong secondary echo to the southwest of the main echo that appears at 565 s and remains present to varying degrees for about 110 s. A frame from the movie that prominently features this structure is shown in Fig. 6. This highlights the benefits of using the TBN mode for probing ionospheric structure on smaller temporal scales. With TBW captures being spaced by a minimum of five minutes, a sequence of TBW captures could easily miss the formation and evolution of such structures. The same is true for most ionosonde systems, which typically use integration times on the order of a minute or more to boost signal-to-noise. As with the TBW captures, second-hop echoes are seen throughout the observation, which vary noticeably in both strength and location due to significantly ionospheric variability.

4. Applications

While the fixed broadcast frequencies used by WWV limit flexibility, the combination of continuously broadcasting, relatively high-power transmitters with the all-sky capability of LWA1 make the combined passive radar system a potentially powerful tool for exploring both ionospheric structure and a variety of OTH targets. Here, we describe examples of the possible applications of the LWA1+WWV radar system.

4.1. Ionospheric Structure and its Impact on Geolocation

The movies of the image cubes made with both the TBW and TBN data illustrate the significant amount of variability within the ionosphere as one can see the first-hop WWV signal move noticeably in the sky. This is likely due to density gradients at the altitude/layer where the signals are reflected, which is one of the know limitations to geolocation precision for operational OTH radar systems [e.g., *Headrick and Thomason*, 1998].

To illustrate this, we have used the TBW data at 10, 15, and 20 MHz to geolocate the WWV transmitters. To do this, we used a kind of center-of-mass computation using the total power as a weight to estimate the observed elevation, azimuth, and range of each TBW capture and frequency when the first-hop echo was detected (detection limits were deduced empirically by eye). Using this type of center-of-mass calculation also allows us to compute estimates for the uncertainties in the sky position and range using estimates of the 1σ error in the measured power for all the images in the cube. We did this by measuring the standard deviation in the center of each image within the cube where there are essentially no WWV or WWVH echoes. These errors were then propagated through the full geolocation calculation described below. In each case, the computation was limited to a rectangular region on the sky (determined by eye) and ranges between 454 and 1658 km.

We then geolocated the signal assuming a virtual mirror approximation [see *Headrick and Thomason*, 1998, and references therein]. In other words, we approximated the ionosphere with a flat mirror, using the determined sky position and range with the laws of cosines and sines to determine the angular separation between LWA1 and the transmitter on the surface of the Earth. While some of the final geolocations have relatively large errors, the typical 1σ uncertainties for significant first-hop detections were 0.007° and 0.01°, or 0.8 and 1 km for the latitudes and longitudes, respectively.

The geolocation results are plotted in Fig. 7. From these, one can immediately see that the measured positions contain a significant amount of scatter and are systematically off from the expected position to the northeast (left panel). The latter is a manifestation of a known pointing error associated with LWA1. While the source of this pointing offset is currently unknown, it fortunately appears to be stable with time and has been well constrained using bright cosmic sources with well-known sky coordinates [see *Dowell and Grimes*, 2012]. After applying the pointing correction described by *Dowell and Grimes* [2012], the mean geolocated position agrees very well with the known WWV location, within 0.03°, or 3.2 km (right panel of Fig. 7).

There is a significant amount of scatter among these positions with an RMS deviation from the expected WWV position of about 0.13° or 14.6 km, more than an order of magnitude larger than the typical measured uncertainty based on the noise in the all-sky images. As noted above, this scatter is likely from density gradients within the ionosphere that work to invalidate the virtual mirror approximation and is consistent with previous measurements of HF bearing errors at midlatitudes [*Tedd et al.*, 1985]. In total, there were 237 separate geolocation measurements, but the error in the mean position, 0.03°, is more than an order of magnitude larger than RMS/$\sqrt{N}$, the result one would expect if the ionospheric errors in the positions were uncorrelated. This suggests that a significant portion of the structures responsible for these position offsets span the typical temporal/spatial scales probed by these observations.

To explore these structures further, we have used a "tilted mirror" approximation, allowing for density gradients in the ionosphere to act as distortions in what would otherwise behave as a flat mirror. We have done this by using the known positions of LWA1 and WWV with the sky position (corrected for the pointing error) and range of each measurement to compute the three dimensional vectors pointing from LWA1 to the virtual point of reflection within the ionosphere, $\vec{r_r}$, and from this point to WWV, $\vec{r_t}$ (see Fig. 8 for a schematic representation). Specifically, $\vec{r_r} = r_r(l\hat{i} + m\hat{j} + \sqrt{1-l^2-m^2}\hat{k})$ where l and m are the direction cosines described Sec. 2.3 (i.e., the sky position measured from the image cube) and r_r is simply the length of $\vec{r_r}$. If we define a vector, $\vec{d}$, that points from LWA1 to WWV such that $\vec{d} = d_x\hat{i} + d_y\hat{j} + d_z\hat{k}$, and note that the length of the path traveled by the signal measured from the image cubes is given by $R = r_r + r_t$, the law of cosines yields the following

$$r_r = \frac{1}{2}\frac{R^2 - d^2}{R - (d_x l + d_y m + d_z\sqrt{1-l^2-m^2})} \quad (1)$$

where $d^2 = d_x^2 + d_y^2 + d_z^2$ and r_t is the length of $\vec{r_t}$. Following this, one can compute $\vec{r_t}$ by noting that $\vec{d} = \vec{r_r} + \vec{r_t}$.

After solving for both $\vec{r_r}$ and $\vec{r_t}$, one can compute the virtual height, h_v, of the ionospheric reflection, i.e., the height above the Earth's surface where $\vec{r_r}$ and $\vec{r_t}$ intersect. The plasma frequency, f_p at this location can also be estimated as $f_p = f\cos\theta/2$, where f is the observing frequency and θ is the angle between $\vec{r_r}$ and $\vec{r_t}$ computed via the dot product of their associated unit vectors, $\hat{r_r}$ and $\hat{r_t}$.

Fig. 9 shows what is essentially a comprehensive ionogram for all three sequences of TBW captures color-coded by frequency with different point styles for different sequences. We have also included results computed using image cubes from the 15-minute TBN observation at 15 MHz. The left panel shows virtual height versus f_p if only the secant law is used, that is, if we assume $h_v = (R/2)\cos(90^\circ - e)$ and $f_p = f\cos(90^\circ - e)$, where e is the elevation of the detected echo. One can see that the linear features in this plot do not at all resemble typical ionograms. However, the right panel shows results using the full geometric computation detailed above, which resemble what one might expect for an ionogram when E_s is present.

The 10 MHz data show a mixture of echoes that probe the general density profile during these observations and those that reflected off E_s layers. The two are identifiable by eye in the plot and we have separated them empirically with a dashed line. The 20 MHz data seem to consist of reflections off the

same E_s layers as the 10 MHz data given that they have similar virtual heights ($\sim$95 km). However, f_p is higher for these echoes (5.5 versus 3 MHz), implying that the 10 MHz data yield something akin to fbEs (the E_s "blanketing" frequency) and the 20 MHz data foEs (the E_s maximum reflected frequency), to use ionogram terminology. The 15 MHz TBW data show reflections from a somewhat higher E_s layer ($h_v \simeq$115 km) with f_p somewhat lower ($\sim$5 MHz) than what was seen at 20 MHz. The 15 MHz TBN data show evidence for an even higher E_s layer ($h_v \simeq$125 km) with f_p comparable with the 20 MHz TBW observations.

The computed vectors $\vec{r_r}$ and $\vec{r_t}$ also allow for a characterization of the ionospheric structure by quantifying both the magnitude and direction of the effective tilt. Following the law of reflection, the normal vector, $\hat{n}$, the vector perpendicular to the reflecting surface, is simply the (normalized) difference between $\hat{r_r}$ and $\hat{r_t}$. However, this difference gives the normal vector in a coordinate system centered on LWA1 rather than the location of the ionospheric reflection. To remedy this, the $\hat{n}$ vector is rotated into a coordinate system with the latitude and longitude of the virtual reflection point as the origin. In this coordinate system, the angle between the vertical axis and $\hat{n}$ and the azimuthal coordinate of $\hat{n}$ give the magnitude and direction of the tilt, respectively. We therefore use these two quantities, tilt and tilt azimuth (measured clockwise from north), to quantify the observed density structures.

Fig. 10 shows the virtual height, plasma frequency, tilt, and tilt azimuth derived from the TBW data as functions of local time, separately for those detections classified as reflecting off E_s layers and those that did not. These use the same color-coding and point styles as Fig. 9. One can see that for these TBW sequences, the 10 MHz signals are only able to penetrate above 150 km in the afternoon/evening, at about 13:00 and between 17:00 and 21:00, local time. The 10 MHz data only seem to be affected by E_s in the late evening between 20:00 and midnight. Reflections from E_s at 15 and 20 MHz were prominent between 16:00 and 23:00. While the E_s heights tend to be relatively stable, f_p seems to increase somewhat between 19:00 and 23:00. During this time period, the tilts for the E_s layers become more erratic, reaching nearly 25°, and are directed mostly to the south. This is comparable to the properties of dense E_s "clouds," which are known to have tilts up to 30° [e.g. *Paul*, 1990]. In general, the observed E_s layers show a larger degree of structure with tilts from a few degrees up to about 15° or more while the tilts measured from non-E_s echoes are a few degrees or less. This is consistent with tilts measured for the midlatitude ionosphere [*Tedd et al.*, 1985] and for E_s [*Paul*, 1990]. This is also reflected in the geolocation results presented above; for E_s echoes, the RMS deviation from the expected WWV position is 0.24°, or 26.5 km; for non-E_s echoes, the RMS geolocation error is 0.076°, or 8.5 km.

For the 15-minute TBN observation at 15 MHz, we have made the same plots as in Fig. 10, but at a much higher temporal resolution, i.e., 1-s versus 10-minutes (see Fig. 11). These show evidence of small time-scale variations in all four quantities. The measured value for h_v seem to suggest the presence of two main E_s layers at heights of roughly 115 and 135 km with plasma frequencies of about 6.2 and 5.5 MHz, respectively. The higher layer has a roughly 5° tilt that gradually evolves from being directed eastward at the start of the observation to northward at the end. The lower layer seems to have a roughly northward-directed tilt of about 12° throughout the observation. The effect of the strong secondary echo shown in Fig. 6 and discussed in Sec. 3.2 can be seen near 17:00 local time as several echoes from lower, denser E_s structures appear with large ($\sim$20°) tilts directed toward the southwest.

4.2. OTH Terrain Mapping

As noted in Sec. 3.1 and 3.2, there are second-hop signals observable at all three frequencies and within both the TBW and TBN data. Given some simplifying assumptions, these can potentially be used to produce maps of HF reflectivity for the distant terrain and/or ocean. In order to locate the point on the terrain/ocean where the second-hop signals reflected, we are forced to make the assumption that both ionospheric hops occurred at the same altitude. This assumption allows us to compute the distance traveled by the WWV signal from the reflection point on the terrain/ocean to LWA1 by simply dividing the total time/distance of flight in half. Then, using the image cubes described in Sec. 3.1 and 3.2, one can map the reflected HF power using a simple virtual mirror approximation (i.e., without tilts). The results presented in Sec. 4.1 suggest that ionospheric structure and variability will introduce geolocation errors of about 0.13°. We can assume that this is increased by

roughly a factor of $\sqrt{2}$ to 0.18° for second-hop data since these signals have reflected off the ionosphere twice. However, for this type of mapping exercise, this is an acceptable level of uncertainty given that the LWA1 beam is much larger. Specifically, the full width at half maximum of the LWA1 beam at 10, 15, and 20 MHz is 15.8°, 10.5°, and 7.9°, respectively.

Something that is a concern for terrain mapping and not the analysis presented in Sec. 4.1 is the effect of sidelobes associated with the LWA1 beam. These are apparent in all of the images presented in Fig. 1–6. Since the analysis in the previous section focussed on finding the centroid of the brightest first-hop signal on the sky, these sidelobes were of little concern. However, as we attempt to map the HF reflectance using the detected power from several different directions at once, confusion from sidelobes will have a significant impact.

Within the field of radio astronomy, an effective iterative approach has been developed to mitigate the consequences of such sidelobes that combines deconvolution and self-calibration. However, these techniques have been designed to work with data from a "multiplying" rather than "adding" interferometer. In other words, they work on images made with visibilities, which are correlations between all possible pairs of antennas, or "baselines." For a baseline with antennas i and j, $V_{i,j} = \langle \varepsilon_i \varepsilon_j^* \rangle$, where V is the visibility, ε is the complex voltage, and the average is performed over a fixed time interval. Images made with such visibilities are equivalent to total-power beam-formed images, but with a constant "DC" term subtracted.

Specifically, the intensity on the sky is related to the visibilities by the following

$$I(l,m) = \iiint V(u,v,w) e^{2\pi i(ul+vm+nw)} du\, dv\, dw \tag{2}$$

where l and m are direction cosines for a particular part of the sky (i.e., not necessarily the zenith as we have used here), $n = \sqrt{1-l^2-m^2}$, and the baseline coordinates, u, v, and w are the differences between the positions of the two antennas of the baseline in a coordinate system such that w points toward the observation field center, u points eastward, and v points northward.

Typically, visibilities are "fringe-stopped" by multiplying them by $\exp(-2\pi i w)$, so that for a small field of view (i.e., $n \approx 1$), the w term can be ignored because $n - 1 \simeq 0$. In this case, the image can be made by gridding the visibilities in the u,v-plane and performing a two-dimensional FFT. For our LWA1 observations, the field of view is far from small. However, because the LWA1 antennas lie nearly within a plane and we have defined the field center of our images at zenith, the w term is still small in our case (i.e., $w \simeq 0$). In addition, as one can see from Fig. 1–6, all of the detected WWV echoes are near the horizon where $n \simeq 0$. Thus, by not fringe-stopping our computed visibilities, we effectively make the nw term in equation (2) negligible and can used a standard FFT-based imager with our LWA1+WWV visibilities.

The scheme used to reduce sidelobe confusion within FFT-based visibility imaging is as follows. After the data are initially calibrated, an image is made and a deconvolution algorithm is applied. The most commonly used algorithm is clean [see *Cornwell et al.*, 1999], which models the image with a series of delta functions, called "clean components," convolved with the impulse response of the interferometer, or "dirty beam." The locations of the clean components are determined iteratively by placing one at the location of the pixel with the largest absolute value and subtracting a scaled version of the dirty beam at that location at each iteration. This process is usually terminated at the first iteration when the pixel with the largest absolute value is actually negative. After this, the clean components are convolved with a Gaussian beam with a width similar to the main lobe of the dirty beam and added back to the residual image.

Following the application of the clean algorithm, the clean components are used as a model of the intensity on the sky to refine the visibility calibration. Within this self-calibration process, antenna-based phase corrections are solved for using a non-linear fit (usually, a gradient search). Because an array with N elements has $N(N-1)/2$ unique baselines, this is generally an overly constrained problem, e.g., for LWA1, one has to solve for 256 phase corrections using 32,640 baselines. Amplitude corrections can also be solved for within this process, but it is usually safer to use phase-only self-calibration to avoid biasing the calibration toward the locations of the clean components. After applying the resulting calibration, the visibilities are re-imaged and clean is run again. Because of improvements in image fidelity made possible by the self-calibration-determined phase corrections, subsequent applica-

tions of clean are able to mitigate the effect of sidelobes to a greater degree. After cleaning, one can repeat self-calibration with the new clean-component model and continue to iterate until the process converges.

To apply these techniques to the TBW and TBN data, visibilities were computed by correlating the complex voltages for each time of arrival over the entire observing period. Visibilities for both polarizations and both side-bands (i.e., carrier frequency $\pm$1000 Hz) were averaged together. For the TBW data, the correlations were computed using all TBW captures and for the TBN data, the entire 15-minute observation was used. This was done separately for each frequency. For each time of arrival and frequency, the visibilities were imaged with three iterations of clean and self-calibration. Additional iterations did not significantly change the appearance of the images produced.

The final cleaned images from the TBW data at each frequency and time of arrival are displayed in Fig. 12. For the purposes of terrain mapping, only times of arrival corresponding to travel distances between 1958 and 4666 km were used to minimize contamination by first-hop WWV signals and echoes of WWVH. Similar images were made from the TBN data, but are not shown here. In Fig. 12, the horizon is indicated in each panel with a grey circle. One can see that sidelobes have been effectively eliminated, particularly around bright echoes. It is also apparent that despite the narrow range in time of arrival used, contamination from WWVH and first-hop WWV echoes is still an issue. For the analysis to follow, polygon regions were drawn by eye around the first-hop WWV echoes at 10, 15, and 20 MHz and around the WWVH echoes at 10 and 15 MHz (recall, WWVH does not broadcast at 20 MHz) to exclude those regions from the terrain mapping process; they are shown in white in Fig. 12. The origin of the strong source significantly beyond the horizon to the east in the 15 MHz is not entirely clear. However, it seems likely that since its strength roughly correlates with the WWVH echo that it is an aliased version of WWVH introduced by our FFT-based imager.

Within each truncated image cube (i.e., only ranges between 1958 and 4666 km), the sky position and range of each cubic pixel was used to compute a latitude and longitude, using the assumptions detailed above. The pixels where then binned into a latitude and longitude grid, and the mean power within each grid cell was computed to produce power maps for each frequency. These are shown in Fig. 13 for the TBW data and in Fig. 14 for the TBN data. For all maps, the regions excluded due to contamination by first-hop WWV echoes are shaded in grey as are the WWVH-excluded regions for the 10 and 15 MHz maps.

One can see that while the 5-ms width of the WWV pulse limits the resolution in the direction radially away from LWA1, there are many distinct features visible. One of the most striking is a strong signal originating from the Gulf of Mexico which is apparent in the 10 and 20 MHz TBW maps, but not in either 15 MHz map. This could be indicative of Bragg scattering from waves in that region with spacings of about 7.5 m. Such waves would produce Bragg scattering at wavelengths of 15 and 30 m (20 and 10 MHz), but not at 20 m (15 MHz).

There is a strong feature originating from the Pacific Ocean to the southwest of the Baja Peninsula within all of the TBW-based maps. The superior azimuthal resolution of the 20 MHz map shows that this feature may consist of two or more Bragg lines. What is likely a similarly strong Bragg line is seen near the Oregon coast in all the TBW maps. These are not seen in the 15 MHz TBN map. The 20 MHz map also shows evidence of substantial reflections from the Pacific Ocean west of California that were not observable at 10 and 15 MHz because of contamination from WWVH echoes.

Both 15 MHz maps as well as the 20 MHz TBW map show strong reflections from the midwestern and plains states, stretching from Minnesota/Wisconsin to eastern Texas. This is likely due to the general lack of rough or mountainous terrain in these regions that would tend to scatter any incident HF signals.

5. Discussion and Conclusions

We have demonstrated that using existing technologies, developed and operated for other purposes, it is possible to construct a relatively powerful, passive OTH radar system. Using the first of many stations of the LWA to observe echoes from the NIST station WWV, we have shown that one can probe and monitor ionospheric structure, map HF reflectivity of land and sea over a large area, and potentially track OTH targets. The all-sky capability of LWA1 allows us to locate and track both single-hop

and multi-hop echoes from WWV in any direction during a variety of ionospheric conditions.

Using preliminary commissioning data, we have been able to demonstrate the impact ionospheric phenomena such as sporadic-E may have on OTH geolocation precision. We have shown that that structures associated with the detected E_s layers persist in time and space such that averaging over many, relatively closely spaced observations does not improve geolocation accuracy as much as one may expect (i.e., by a factor of $\sqrt{N}$). As more LWA stations are added, continued observations of WWV will allow us to establish a kind of coherence scale length, the separation beyond which ionospheric structures of a given type are uncorrelated. Beyond this scale, the geolocation errors added by different parts of the ionosphere will likewise be uncorrelated such that one may achieve a $\sqrt{N}$ improvement in accuracy by averaging the results from N stations independently observing the same OTH signal and spaced a minimum of the coherence length apart from one another. For example, by using 10 stations spaced in this manner, the RMS geolocation error reported here of 14.6 km would be reduced to 4.6 km and would be achieved in real-time (i.e., by averaging over space rather than time).

In light of the results presented here, having many LWA stations observing WWV would also be a powerful probe of ionospheric structure, especially within E_s layers. The techniques described here and elsewhere [e.g. *Paul*, 1990] allow one to estimate the ionospheric tilt at a particular location within the ionosphere. Having multiple stations with independent lines of sight capable of observing simultaneously at 10, 15, and 20 MHz will allow for detailed three-dimensional maps of E_s layer structure, which can be monitored as a function of time.

The ocean/terrain mapping capability of this system will also be enhanced with multiple stations by improving sensitivity and location accuracy. This may be important for possible real-time applications such as monitoring wave activity and currents simultaneously in the Gulf of Mexico and the Pacific Ocean via Bragg scatter of the HF signals.

Acknowledgments. The authors would like to thank F. Schinzel and T. Pedersen for useful comments and suggestions. Basic research in astronomy at the Naval Research Laboratory is supported by 6.1 base funding. Construction of the LWA has been supported by the Office of Naval Research under Contract N00014-07-C=0147. Support for operations and continuing development of the LWA1 is provided by the National Science Foundation under grand AST-1139974 of the University Radio Observatory program. Part of this research was carried out at the Jet Propulsion Laboratory, California Institute of Technology, under a contract with the National Aeronautics and Space Administration.

References

Cornwell, T., R. Braun, and D. S. Briggs (1999), Deconvolution, in *Synthesis Imaging in Radio Astronomy II, ASP Conference Ser.*, vol. 180, edited by G. B. Taylor, C. L. Carilli, and R. A. Perley, pp. 151–170, ASP, San Francisco, Calif.

Cornwell, T. and E. B. Fomalont (1999), Self-Calibration, in *Synthesis Imaging in Radio Astronomy II, ASP Conference Ser.*, vol. 180, edited by G. B. Taylor, C. L. Carilli, and R. A. Perley, pp. 187–199, ASP, San Francisco, Calif.

Dowell, J., D. Wood, K. Stovall, P. S. Ray, T. Clarke, G. Taylor (2012), The Long Wavelength Array Software Library, *J. Astro. Inst., 1*, id. 1250006, doi: 10.1142/S2251171712500067

Dowell, J. and C. Grimes (2012), LWA1 Pointing Error and Correction, Long Wavelength Array Memo 194, Oct. 2, 2012 `http://www.ece.vt.edu/swe/lwa/`

Ellingson, S. W. (2007), Transient Buffer - Wideband (TBW) Preliminary Design, Long Wavelength Array Memo 109, Nov. 11, 2007 `http://www.ece.vt.edu/swe/lwa/`

Ellingson, S. W., et al. (2012), The LWA1 Radio Telescope, *IEEE Trans. Ant. Prop.*, submitted, Long Wavelength Array Memo 186, Aug. 22, 2012 `http://www.ece.vt.edu/swe/lwa/`

Headrick, J. M., and J. F. Thomason (1998), Applications of high-frequency radar, *Rad. Sci., 33*, 1405–1054

Hicks, B. C., et al. (2012), A Wide-Band, Active Antenna System for Long Wavelength Radio Astronomy, *Pub. Ast. Soc. Pac., 124*, 1090–1104

Meyer, M. G. and J. D. Sahr (2004), *Rad. Sci., 39*, 39, RS3008, doi:10.1029/2003RS002985

Nelson, G. K., M. A. Lombardi, and D. T. Okayama (2005), NIST Time and Frequency Radio Stations: WWV, WWVH, and WWVB, *National Institute of Standards and Technology Special Publication 250-67*

Paul, A. K. (1990), On the variability of sporadic E, *Rad. Sci., 25*, 49–60

Taylor, G. B., et al. (2012), First Light for the First Station of the Long Wavelength Array, *J. Astro. Inst., 1*, id. 1250004, doi: 10.1142/S2251171712500043

Taylor, G. B., et al. (2006), LWA Overview, Long Wavelength Array Memo 194, Oct. 2, 2012 `http://www.ece.vt.edu/swe/lwa/`

Tedd, B. L., H. J. Strangeways, and T. B. Jones (1985), Systematic ionospheric electron density tilts (SITs) at mid-latitudes and their associated HF bearing errors, *J. Atmos. Terr. Phys., 47*, 1085–1097

J. F. Helmboldt, US Naval Research Laboratory, Code 7213, 4555 Overlook Ave. SW, Washington, DC 20375 (joe.helmboldt@nrl.navy.mil)

(Received _____.)

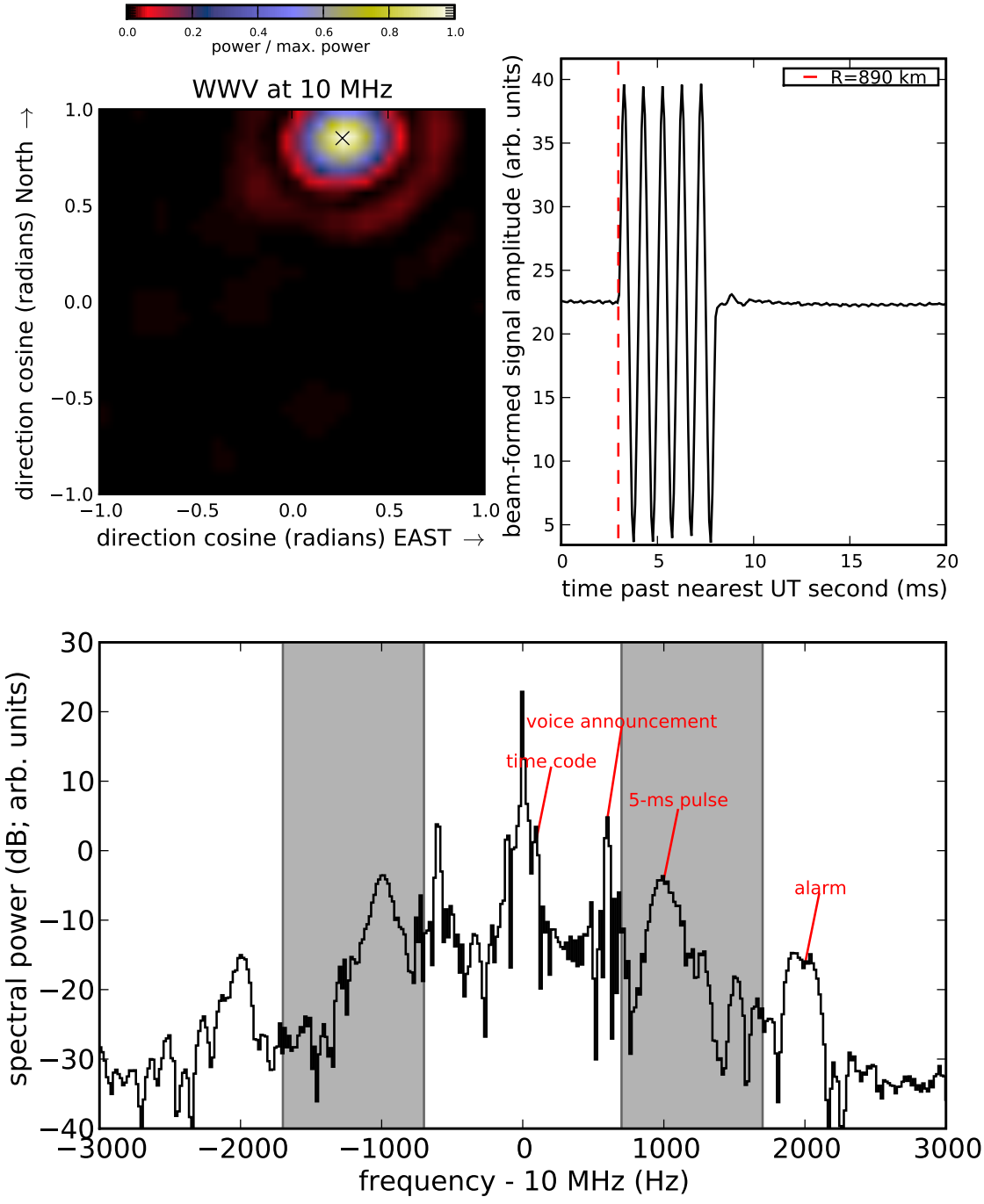

Figure 1. An all-sky image made at 10 MHz from a single TBW capture (see Sec. 2) showing the ionospheric echo of WWV (upper left), the amplitude of the beam-formed signal toward the center of the echo marked with an × in the image to the left (upper right), and the power spectrum of the beam-formed signal (lower) with grey shaded regions representing the filter used to isolate the 5-ms, on-the-second pulse.

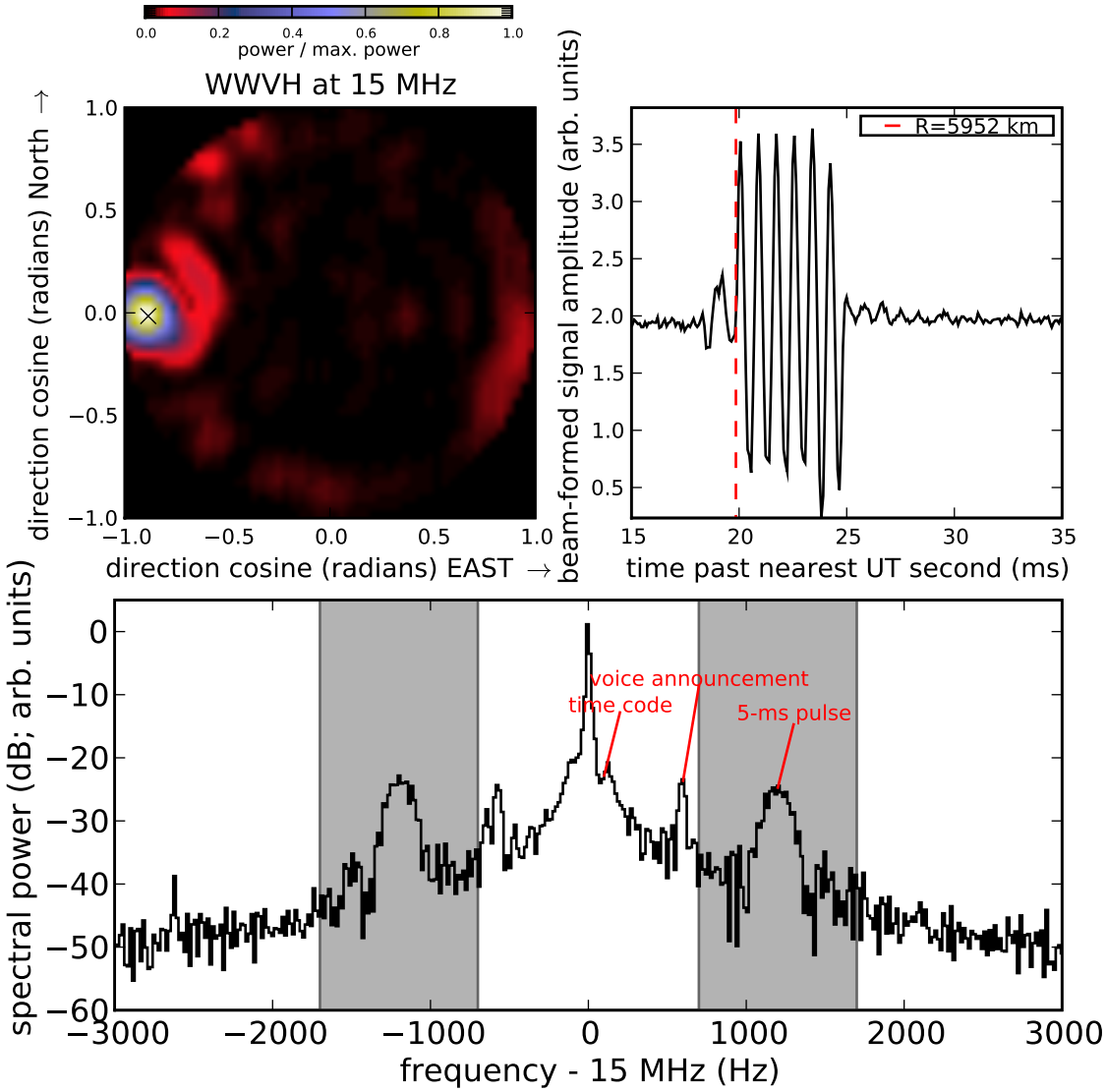

Figure 2. The same as Fig. 1, but at 15 MHz, showing the detection of an echo from WWVH using the same TBW capture.

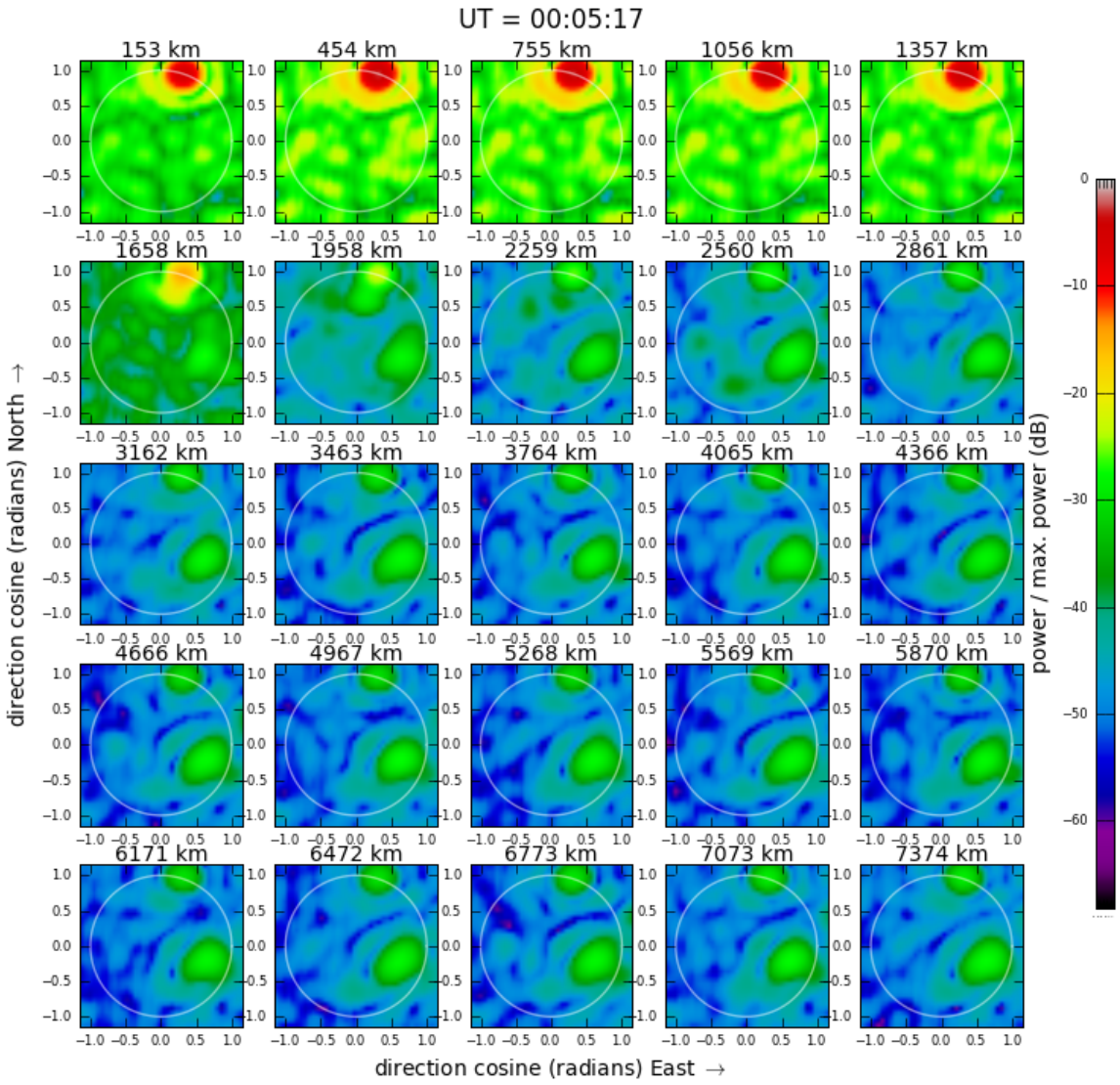

Figure 3. An example of an all-sky/range image cube from the 10 MHz WWV signal with a single TBW capture. The white circle indicates the horizon/field of regard. This is the first frame of a movie of three separate sequences of such captures, which is available electronically.

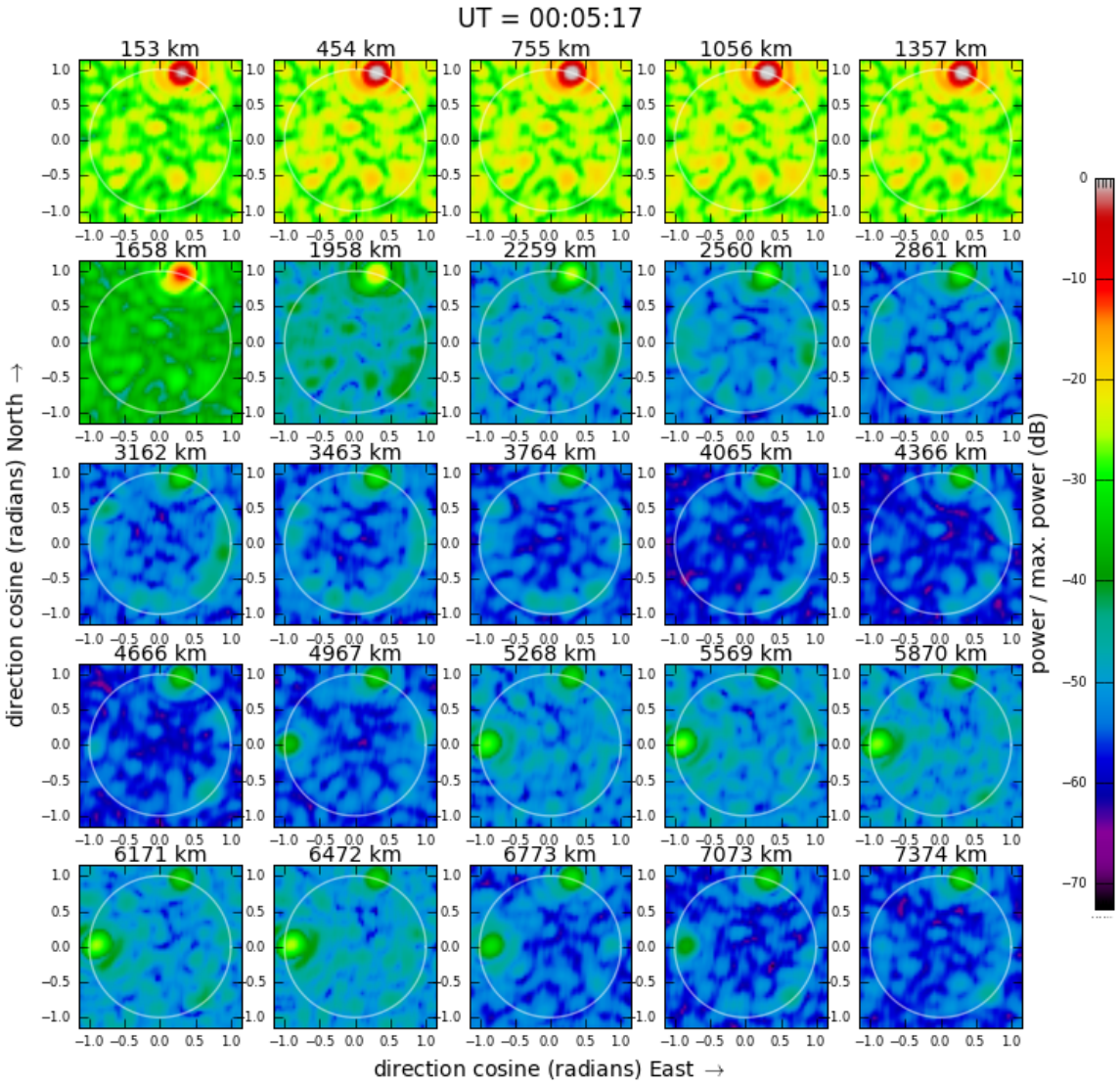

Figure 4. The same as Fig. 3, but using the 15 MHz signal from the same TBW capture. This is also the first frame of a movie of three separate sequences of such captures, which is available electronically.

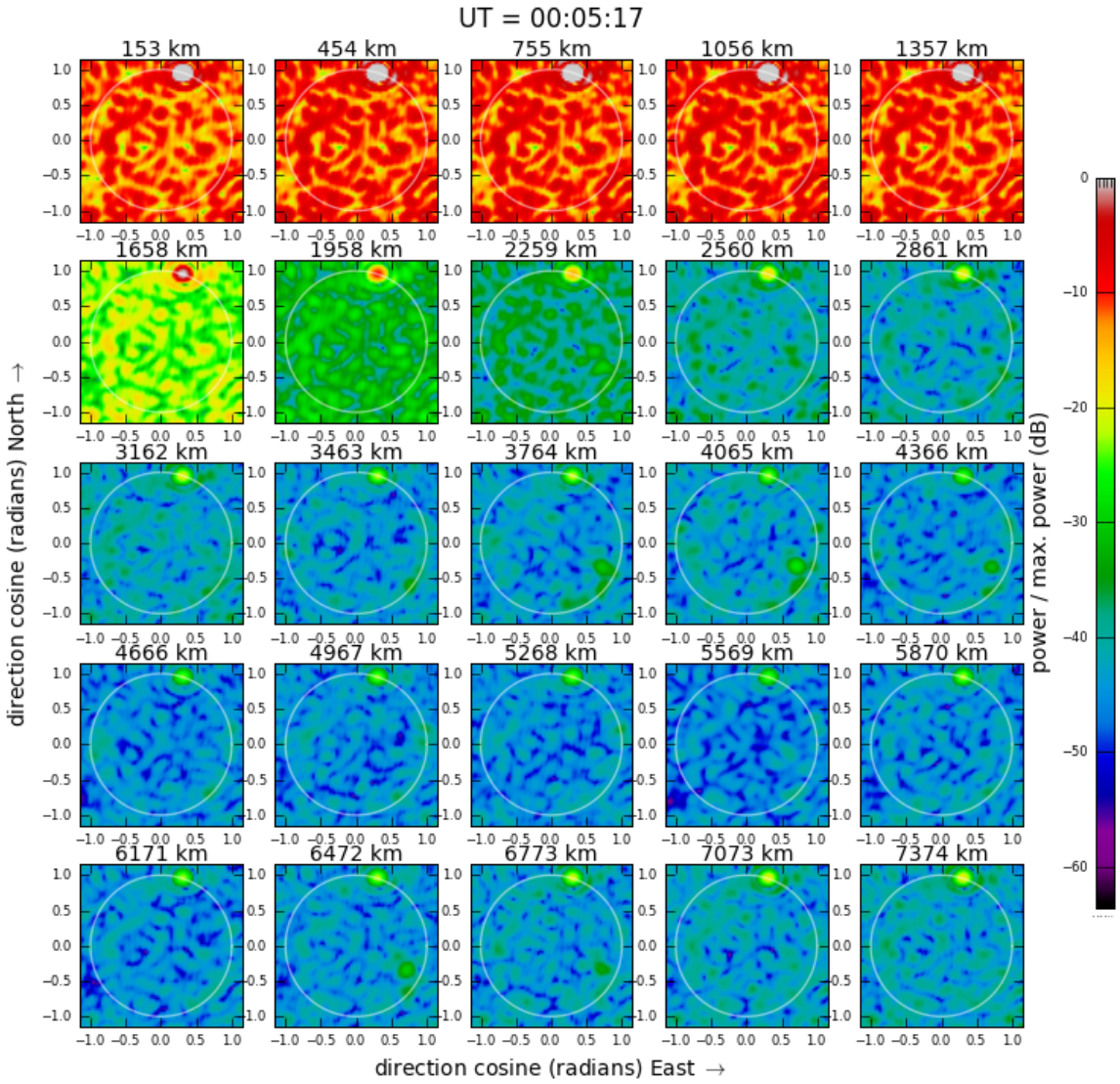

Figure 5. The same as Fig. 3, but using the 20 MHz signal from the same TBW capture. This is also the first frame of a movie of three separate sequences of such captures, which is available electronically.

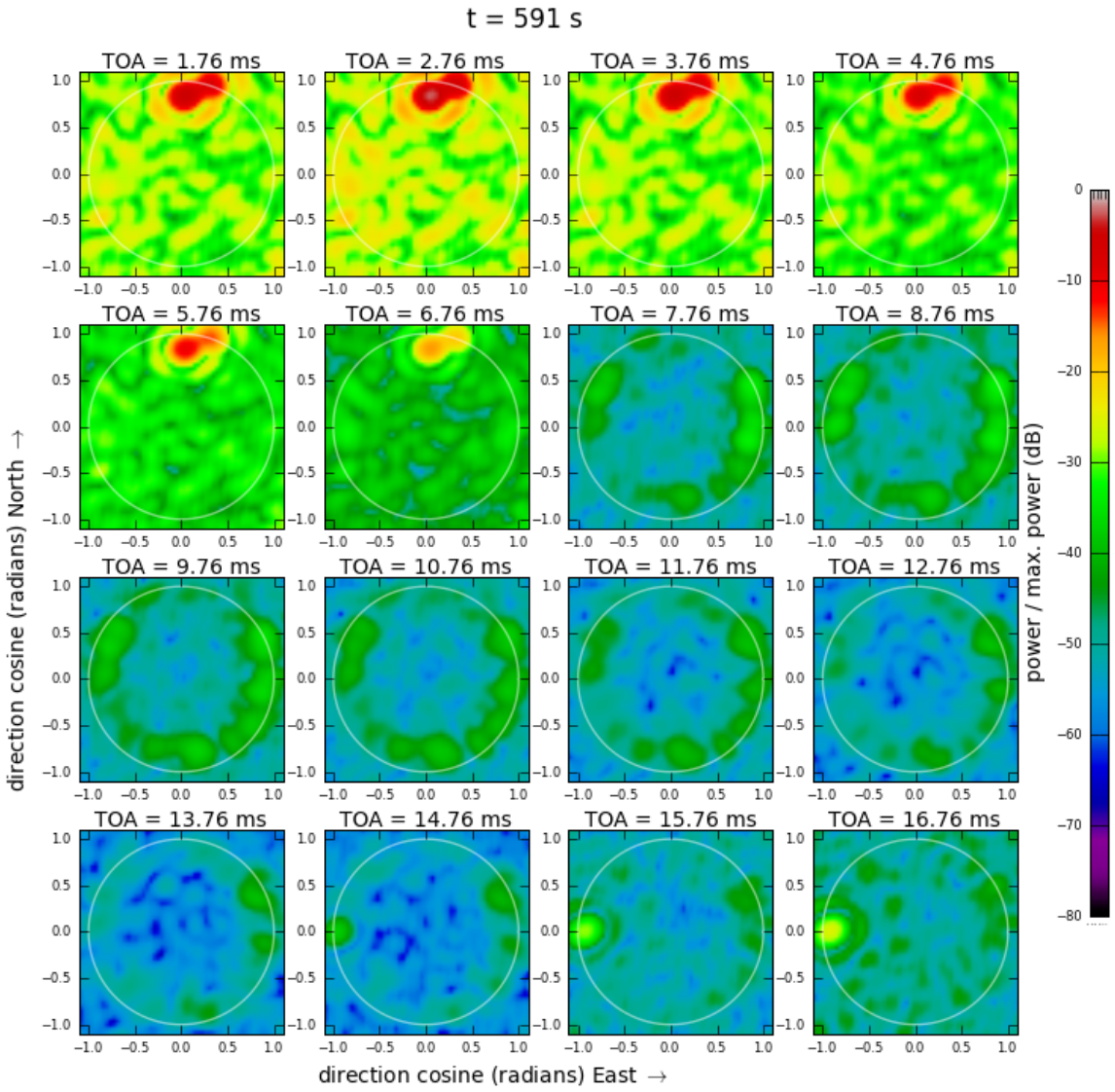

Figure 6. An all-sky/time-of-arrival image cube from one second of a 15-minute TBN observation at 15 MHz starting at 00 UT on 25 Sep. 2012. As in Fig. 3–5, the white circle indicates the horizon/field of regard. This is a frame from a movie (roughly 2/3 from the beginning) that covers the entire 15 minute TBN observation and which is available electronically.

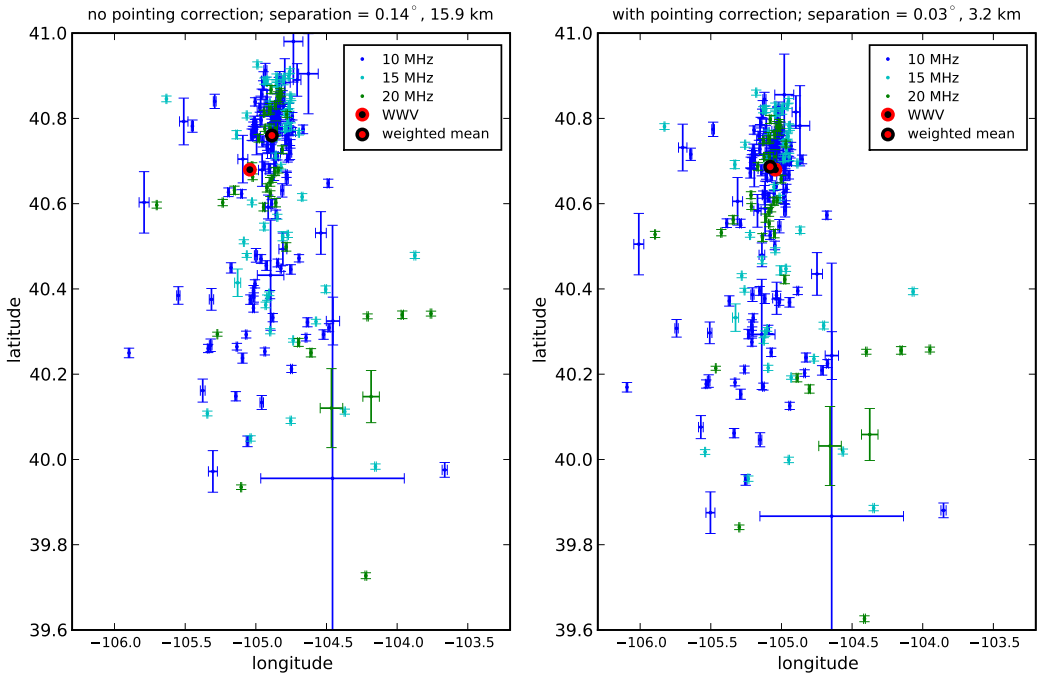

Figure 7. Geolocation of the WWV transmitter(s) using detections of echoes at 10, 15, and 20 MHz from TBW captures using a standard virtual mirror approximation. The two panels show the results before (left) and after (right) the LWA1 pointing correction was applied (see Sec. 4.1).

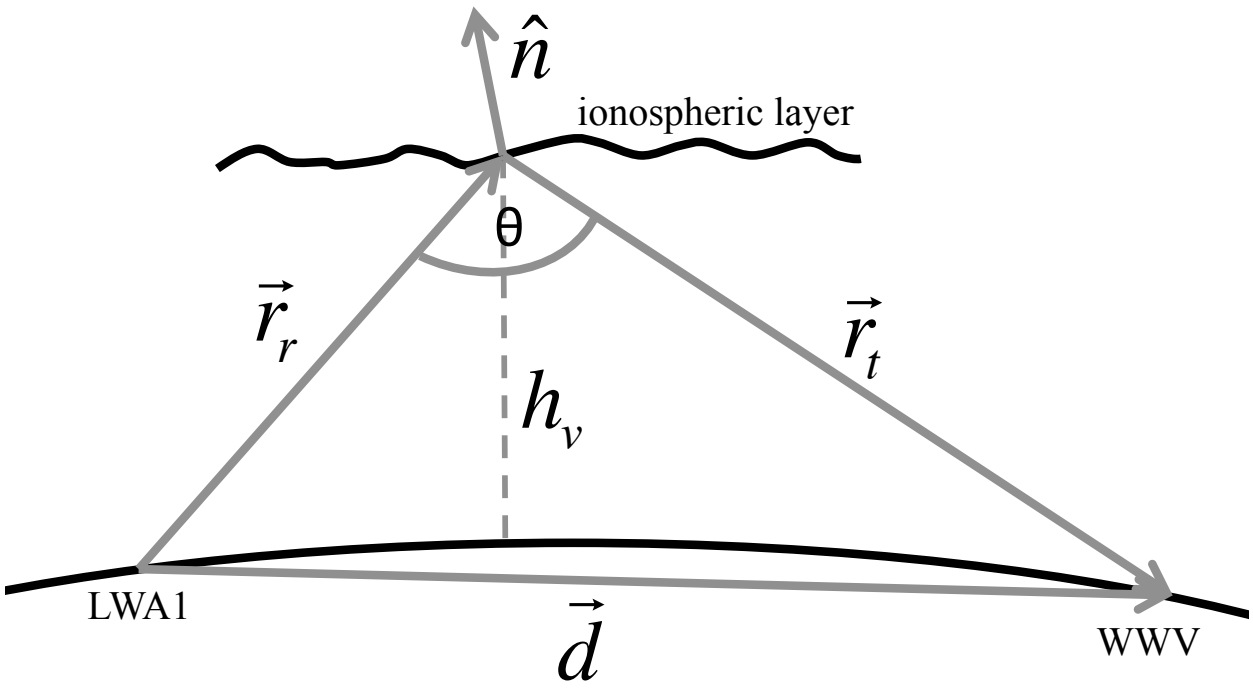

Figure 8. A schematic representation (not to scale) of the vector computations used to locate the point of reflection in a tilted virtual mirror approximation. The vector notations are described along with the calculations in Sec. 4.1.

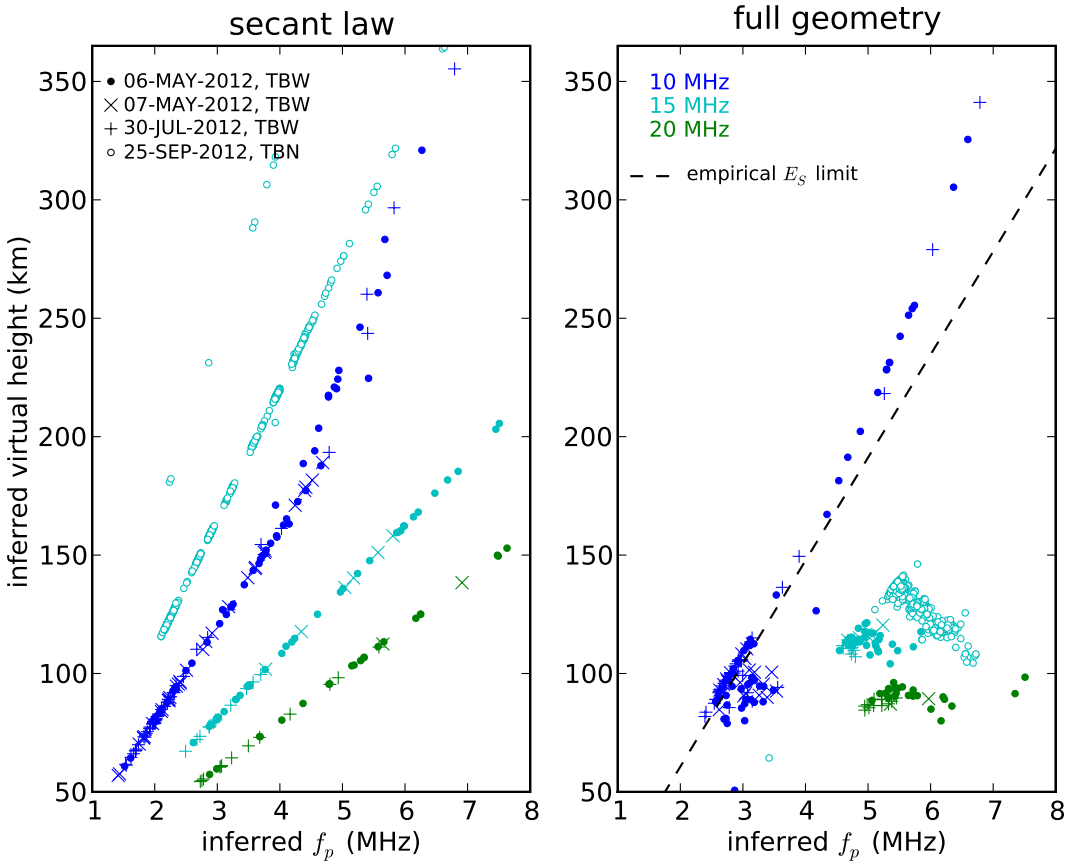

Figure 9. Using all TBW and TBN observations, reconstructed ionograms, using a virtual mirror approximation. The left panel shows the result when only the secant law is assumed, and the right panel displays the computed parameters when the full geometry is taken into account, allowing for tilts within the virtual mirror approximation. Point styles indicate which data were taken from which dates/observing modes (see upper left corner of the left panel) and colors indicate observing frequency (see upper left corner of the right panel). The empirical separation between sporadic-E (E_s) and the general ionospheric density profile is shown with a dashed line in the right panel.

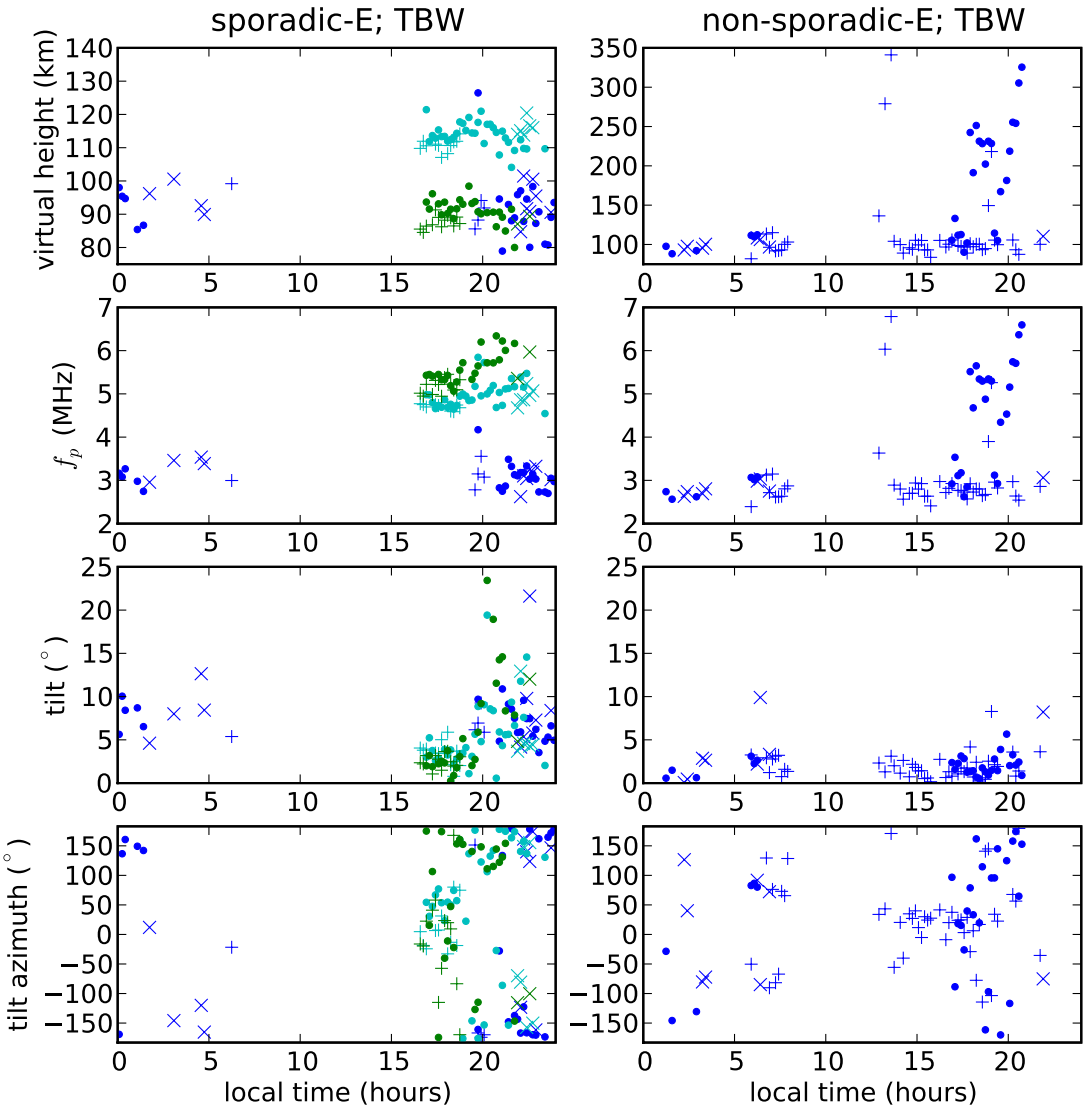

Figure 10. From TBW observations, the derived virtual height, plasma frequency, east-west tilt (derivative of altitude with respect to east-west distance), and north-south tilt (derivative of altitude with respect to north-south distance) as functions of local time. Results for data designated as E_s (see Sec. 4.1 and Fig. 9) are shown on the left; those resulting from the general ionospheric density profile (10 MHz only) are shown on the right. The point styles and color-coding are the same as were used in Fig. 9.

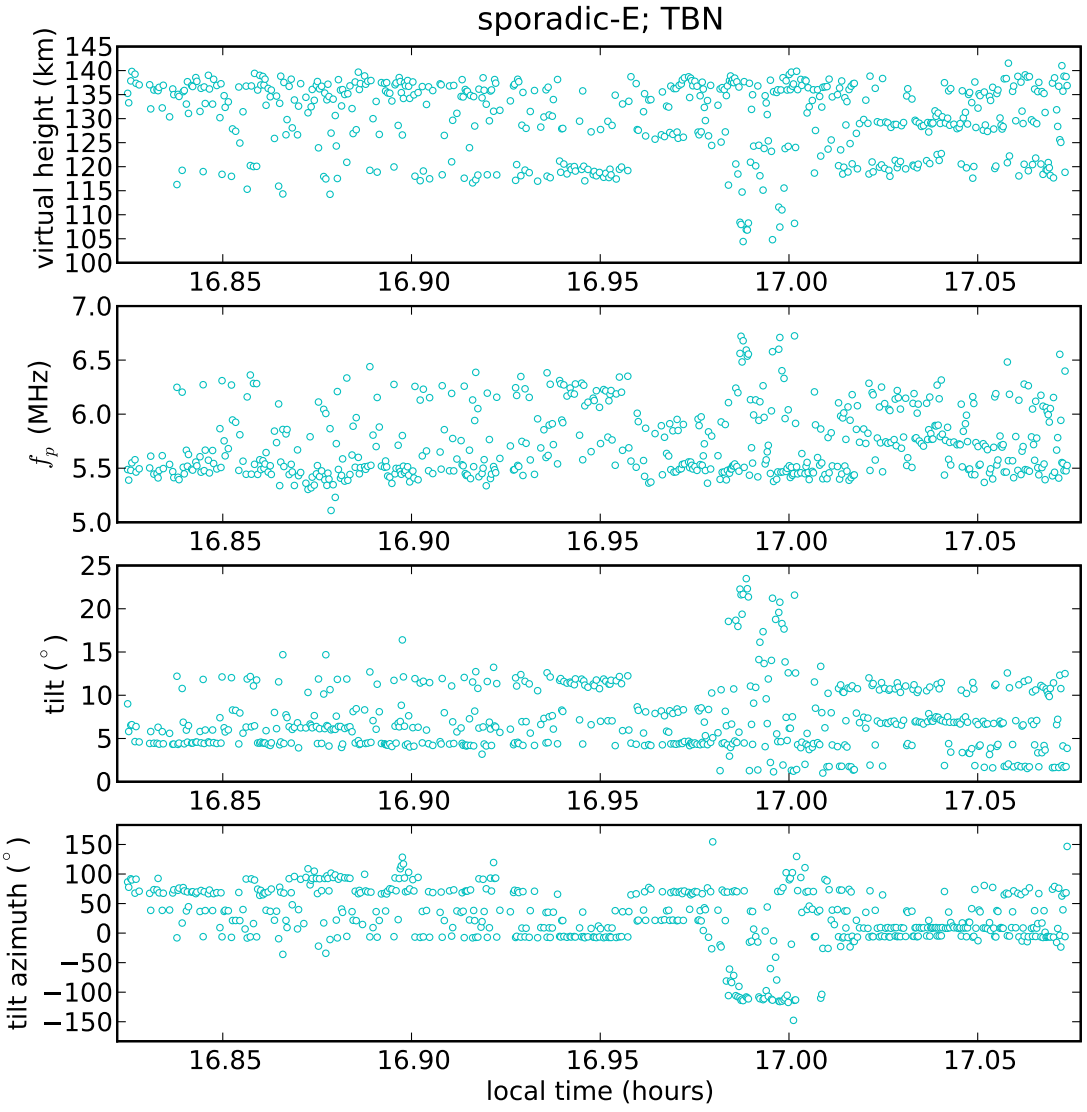

Figure 11. The same as Fig. 10, but for the 15-minute, 15 MHz TBN observation conducted on 25 Sep. 2012. For this observation, all the reflections were from E_s, as was the case for the 15 MHz TBW observations. The point style and color-coding is the same as was used in Fig. 9.

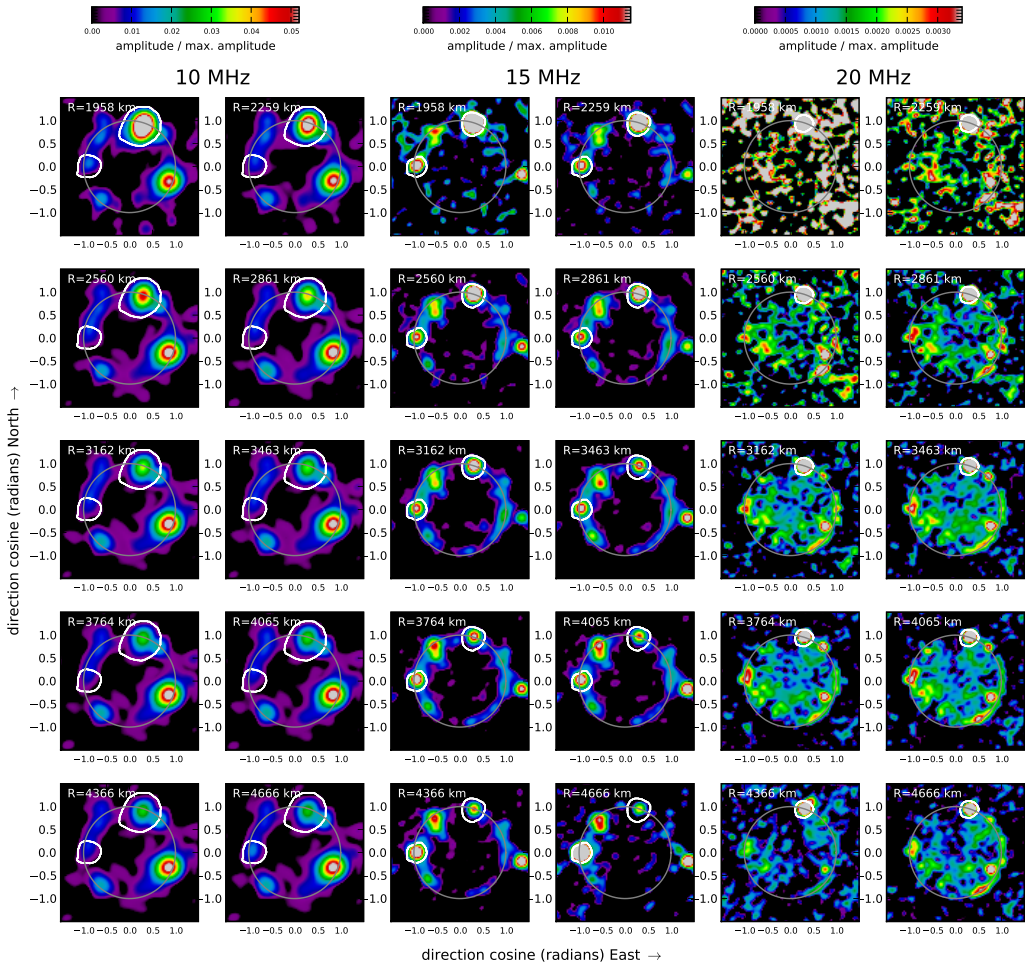

Figure 12. Average all-sky images from all TBW captures at 10, 15, and 20 MHz for ranges consistent with second-hop signals from WWV, i.e., too large to be first-hop signals and too small to be from WWVH. Regions used to exclude contamination by first-hop WWV signals and echoes from WWVH from terrain mapping are shown with white polygons.

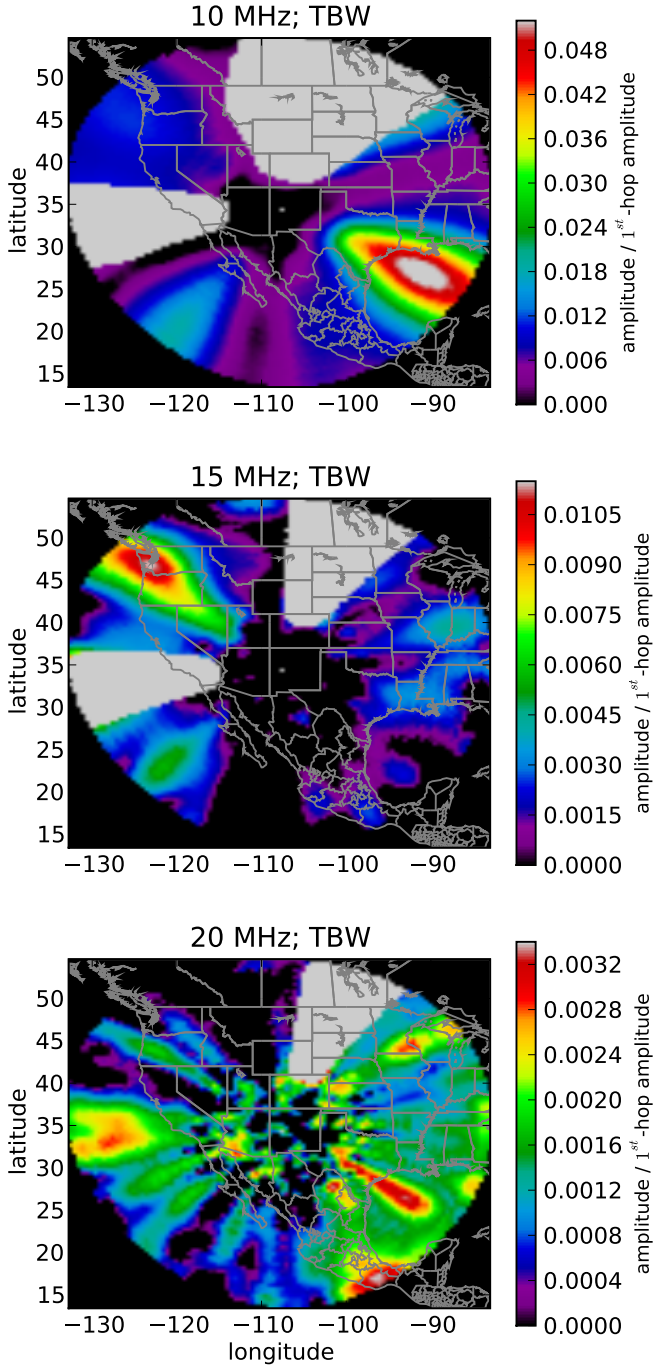

Figure 13. Terrain maps made from the TBW-based images shown in Fig. 12. Regions excluded to minimize contamination by first-hop WWV signals and echoes from WWVH are flagged in light grey.

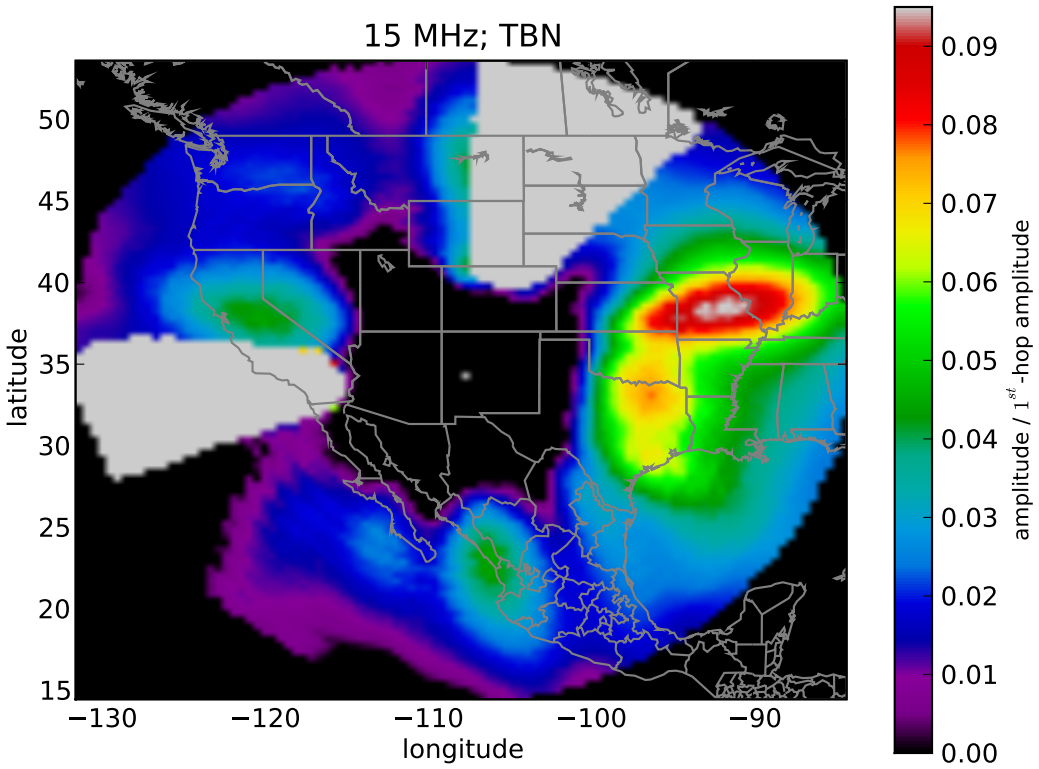

Figure 14. The same as Fig. 13, but for the 15-minute, 15 MHz TBN observation conducted on 25 Sep. 2012.